JOURNAL OF GEOPHYSICAL RESEARCH: SOLID EARTH, VOL. 118, 5453–5466, doi:10.1002/jgrb.50379, 2013

The 5 September 2012 Nicoya, Costa Rica M_w 7.6 earthquake rupture process from joint inversion of high-rate GPS, strong-motion, and teleseismic *P* wave data and its relationship to adjacent plate boundary interface properties

Han Yue,[1] Thorne Lay,[1] Susan Y. Schwartz,[1] Luis Rivera,[2] Marino Protti,[3] Timothy H. Dixon,[4] Susan Owen,[5] and Andrew V. Newman[6]

Received 15 March 2013; revised 16 September 2013; accepted 18 September 2013; published 22 October 2013.

[1] On 5 September 2012, a large thrust earthquake (M_w 7.6) ruptured a densely instrumented seismic gap on the shallow-dipping plate boundary beneath the Nicoya Peninsula, Costa Rica. Ground motion recordings directly above the rupture zone provide a unique opportunity to study the detailed source process of a large shallow megathrust earthquake using very nearby land observations. Hypocenter relocation using local seismic network data indicates that the event initiated with small emergent seismic waves from a hypocenter ~10 km offshore, 13 km deep on the megathrust. A joint finite-fault inversion using high-rate GPS, strong-motion ground velocity recordings, GPS static offsets, and teleseismic *P* waves reveals that the primary slip zone (slip > 1 m) is located beneath the peninsula. The rupture propagated downdip from the hypocenter with a rupture velocity of ~3.0 km/s. The primary slip zone extends ~70 km along strike and ~30 km along dip, with an average slip of ~2 m. The associated static stress drop is ~3 MPa. The seismic moment is 3.5×10^{20} Nm, giving $M_w = 7.6$. The coseismic large-slip patch directly overlaps an onshore interseismic locked region indicated by geodetic observations and extends downdip to the intersection with the upper plate Moho. At deeper depths, below the upper plate Moho, seismic tremor and low-frequency earthquakes have been observed. Most tremor locates in adjacent areas of the megathrust that have little coseismic slip; a region of prior slow slip deformation to the southeast also has no significant coseismic slip or aftershocks. An offshore locked patch indicated by geodetic observations does not appear to have experienced coseismic slip, and aftershocks do not overlap this region, allowing the potential for a comparable size rupture offshore in the future.

Citation: Yue, H., T. Lay, S. Y. Schwartz, L. Rivera, M. Protti, T. H. Dixon, S. Owen, and A. V. Newman (2013), The 5 September 2012 Nicoya, Costa Rica M_w 7.6 earthquake rupture process from joint inversion of high-rate GPS, strong-motion, and teleseismic *P* wave data and its relationship to adjacent plate boundary interface properties, *J. Geophys. Res. Solid Earth*, *118*, 5453–5466, doi:10.1002/jgrb.50379.

1. Introduction

[2] On 5 September 2012, a large shallow-dipping thrust event (M_w 7.6) partially ruptured the plate boundary megathrust fault beneath the Nicoya Peninsula, Costa Rica (Figure 1). An inland and relatively deep hypocenter was reported by the USGS (10.085°N, 85.315°W, 35 km, 14:42:07 UTC; http://comcat.cr.usgs.gov/earthquakes/eventpage/pde20120905144207800_35#summary), as shown in Figure 1. Teleseismic W-phase inversions also indicate a relatively deep (30–40 km) centroid depth (USGS) [*Ye et al.*, 2013], and the global CMT (GCMT) depth was ~30 km (http://www.globalcmt.org/CMTsearch.html). Given the relatively well-constrained regional plate boundary geometry [e.g., *DeShon et al.*, 2006], these depth estimates suggest rupture under the northeastern part of the peninsula, which is somewhat at odds with the strongest shaking (Modified Mercalli Scale Intensity X) being felt in the town of Nosara, 6 km from the Pacific coast.

Additional supporting information may be found in the online version of this article.

[1]Department of Earth and Planetary Sciences, University of California, Santa Cruz, California, USA.
[2]Institut de Physique du Globe de Strasbourg, Université de Strasbourg/CNRS, Strasbourg, France.
[3]Observatorio Vulcanológica y Sismológico de Costa Rica, Universidad Nacional, Heredia, Costa Rica.
[4]Department of Geology, University of South Florida, Tampa, Florida, USA.
[5]Jet Propulsion Laboratory, Pasadena, California, USA.
[6]School of Earth and Atmospheric Sciences, Georgia Institute of Technology, Atlanta, Georgia, USA.

Corresponding author: H. Yue, Department of Earth and Planetary Sciences, University of California, 1156 High St., Santa Cruz, CA 95064, USA. (johnyuehan2003@gmail.com)

2169-9313/13/10.1002/jgrb.50379

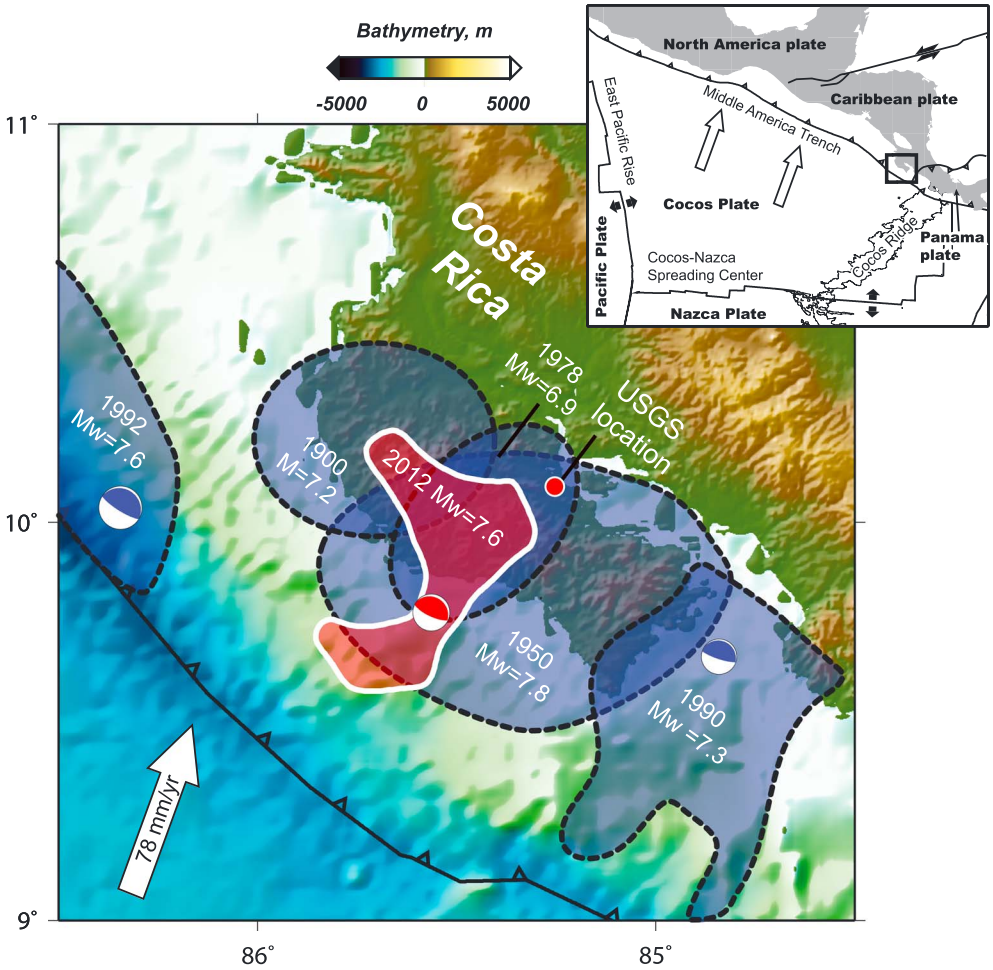

Figure 1. Maps of the study area and regional plate tectonic setting. The inset map locates the Cocos Plate which subducts beneath the North America, Caribbean, and Panama plates along the Middle America Trench. Spreading and transform plate boundaries are marked by solid lines with black arrows indicating relative plate motion. Trenches are marked with barbed solid lines. The Cocos Plate motion relative to the North American and Caribbean Plates is indicated by white arrows. The box identifies the Nicoya peninsula of Costa Rica that is enlarged in the main map. Global centroid-moment tensor solutions are shown for the 5 September 2012 Nicoya, Costa Rica M_w 7.6 event (red filled beach ball) and the 1992 $M_w = 7.6$ and 1990 $M_w = 7.3$ events (blue-filled beach balls). The coseismic region of the 2012 event is indicated with the red-filled patches. The coseismic slip > 1.2 m regions are outlined with solid white curves. Aftershock areas of 1992, 1990, 1978, and 1950 events are indicated with blue-filled patches. Estimated rupture area of 1900 event is also indicated with blue-filled patches. The relative plate motion direction and rate of the Cocos plate is indicated by the white arrow.

[3] Numerous deployments of seismic and geodetic instruments have been conducted over the entire Nicoya Peninsula during the last decade [e.g., *Norabuena et al.*, 2004; *Outerbridge et al.*, 2010] motivated by both the unusual opportunity to place stations on land above a relatively shallow megathrust and by concerns about the regional seismic hazard. The last major earthquake in the Nicoya region was in 1950 (M_s 7.7, $M_w \sim 7.8$), implying that up to 5 m of slip deficit may have accumulated. Many stations were operating during the 2012 earthquake including high-rate GPS (hr-GPS) with ground position solutions computed at five samples per second (sps), and low-rate (one sample per 15 s) GPS (lr-GPS), strong ground motion, broadband, and short-period seismic networks [*Dixon et al.*, 2013]. We utilize these regional observations along with teleseismic body waves to study the main shock rupture process and to compare the slip distribution to prior characterizations of megathrust failure processes.

[4] With steadily improving accuracy over the last decade, hr-GPS time series allow inversion of the space-time rupture history of large earthquakes [e.g., *Miyazaki et al.*, 2004; *Ji et al.*, 2004; *Yue and Lay*, 2011]. The main advantage is that both time-varying (seismic wave motions) and static ground deformations can be modeled in a self-consistent fashion, which yields improved inversion stability compared to teleseismic-signal-only inversions. However, prior hr-GPS finite-fault inversion studies for large megathrust events have been constrained by having one-sided (land side only) station distributions, relatively far from offshore rupture zones, reducing the along-dip slip resolution. This limitation can

be partly compensated by joint inversion with teleseismic datasets, with improved resolution achieved by combining the relative advantages of both near-field and teleseismic observations [*Ammon et al*., 2011; *Yue and Lay*, 2013; *Wei et al*., 2012; *Koketsu et al*., 2011]. However, substantial uncertainty in coseismic slip location remains. For the Nicoya Peninsula, geodetic and seismic networks are directly above and around the main rupture area of the 2012 Costa Rica event (Figure 1) offering unusually good resolution of the space-time history of the rupture process. Comparable resolution has been obtained for earlier megathrust deformation processes around the Nicoya Peninsula, including accumulation of seismic slip deficits, seismic tremor, slow slip events, and microseismic and aftershock distributions, as summarized in the next section.

2. Regional Tectonic Setting and Megathrust Observations

[5] The Nicoya Peninsula protrudes about 60 km seaward over the megathrust plate boundary, where the Cocos plate underthrusts the Caribbean plate at a convergence rate of ~78 ± 1 mm/yr (Figure 1) [*DeMets et al*., 2010; *Protti et al*., 2012]. There are only a few other subduction zones where peninsulas or fore-arc islands (e.g., the Mentawai Islands offshore of Sumatra) provide land access as close as 50–60 km to a deep trench. Beneath the Nicoya Peninsula, there is an along-strike change in the origin of the subducting Cocos plate lithosphere. Lithosphere subducting beneath northwestern Nicoya was formed at the East Pacific Rise (EPR), while lithosphere subducting beneath southeastern Nicoya was formed at the Cocos Nazca spreading center (CNS). Sea floor magnetic anomalies suggest a young age for both lithospheres at the trench, ~24 myr for EPR, and decreasing from 22 to 15 myr southeast toward the Cocos Ridge for CNS [*Barckhausen et al*., 2001; *LaFemina et al*., 2009]. There is a strong variation in heat flux across this lithospheric boundary, from 20–40 mW/m^2 in EPR crust to 105–115 mW/m^2 in CNS crust. This heat flux as well as an upper plate seismic velocity contrast across the EPR-CNS lithospheric boundary [*Audet and Schwartz*, 2013] may influence frictional properties along the megathrust near the peninsula [e.g., *Harris and Wang*, 2002; *Newman et al*., 2002; *Spinelli and Saffer*, 2004].

[6] Several large historic earthquakes have ruptured the megathrust near the Nicoya Peninsula. The 25 March 1990 M_w 7.3 (CMT) earthquake ruptured the offshore region southeast of the Nicoya Peninsula [*Protti et al*., 1995], and the 2 September 1992 shallow M_w 7.6 Nicaragua tsunami earthquake ruptured along the subduction zone northwest of the Nicoya Peninsula [*Kanamori and Kikuchi*, 1993; *Ihmlé*, 1996]. These events bracketed a seismic gap beneath the Nicoya Peninsula ~150 km wide (Figure 1). The 1990 rupture zone may have previously ruptured in 1939 in an M_s 7.3 event. Three recorded large earthquakes ruptured beneath the Nicoya Peninsula in the twentieth century: the 21 June 1900 M ~7.2 event, the 5 October 1950 M_s 7.7, M_w ~7.8 event, and the 23 August 1978 M_w = 6.9 event (Figure 1) [*Pacheco and Sykes*, 1992; *Protti et al*., 2001; *Avants et al*., 2001; *Norabuena et al*., 2004; *Allen et al*., 2009]. The large 1900 and 1950 events have very uncertain rupture zones, which may overlap beneath the central Nicoya Peninsula, with the smaller 1978 event also located in the corresponding region (Figure 1). *Nishenko* [1991] notes other large events likely located under Nicoya in 1827, 1853, 1863, and 1916 and infers that this is one of the most active seismic regions of Costa Rica. Large events under Nicoya have a recurrence time of ~28–50 year, depending on assumptions about rupture overlap. Warnings about the increasing risk of a large megathrust earthquake striking Nicoya have been issued for more than two decades [e.g., *González-Salas and Protti-Quesada*, 2005; *Lundgren et al*., 1999; *Nishenko*, 1991; *Protti et al*., 1995; *Protti et al*., 2001; *Pacheco and Sykes*, 1992; *Iinuma et al.*, 2004; *Feng et al*., 2012].

[7] Regional seismicity beneath the Nicoya Peninsula has been examined using a local on-land and offshore combined broadband/short-period seismic network [e.g., *Newman et al*., 2002; *DeShon et al*., 2006] and suggests an updip limit of the seismogenic zone that deepens from near 15 km depth in the south to 20 km in the north. *Newman et al*. [2002] suggest that this is related to the thermal contrast of the underthrust CNS versus EPR oceanic crust. Other types of deformation are also reported around the Nicoya Peninsula, including transient slow slip events [*Outerbridge et al*., 2010; *Jiang et al*., 2012], deep low-frequency [*Brown et al*., 2009] and very low frequency [*Walter et al*., 2011] earthquakes, and nonvolcanic tremor [*Outerbridge et al*., 2010; *Walter et al*., 2011]. This background activity is not releasing all strain in the subduction zone; geodetic observations indicate spatially varying interseismic coupling, with a concentrated slip-deficit area under the coastal region of central Nicoya Peninsula [e.g., *Iinuma et al*., 2004; *Lundgren et al*., 1999; *Norabuena et al*., 2004; *Feng et al*., 2012]. The most recent of these studies suggests that total locking was present below the central Nicoya Peninsula for at least a decade prior to 2012. Assuming this behavior characterized earlier periods, at least 3 m of slip could have accumulated since 1978 and even more in the surrounding region that ruptured in 1950.

[8] It is generally accepted that large interplate events are likely to rupture previously locked sections of the megathrust; thus, it is reasonable to anticipate that the 2012 Costa Rica event should have ruptured the slip-deficit region imaged by *Feng et al*. [2012]. Initially, it was surprising to note that the inland, relatively deep hypocenter reported by the USGS appeared to be distinct from the locked patch, colocating with a downdip region of low-frequency earthquakes and tremor which is assumed to be weakly seismically coupled. We exploit the high-quality data from the Nicoya Peninsula to evaluate just how close the correspondence is between the prior slip-deficit and coseismic regions and the relationship of the coseismic slip region to regions of tremor and slow slip. Slip zones of recent large earthquakes such as the 2010 Chile (M_w 8.8) and 2011 Tohoku earthquakes (M_w 9.0) have been compared with prior estimates of slip-deficit patterns, but the offshore spatial resolution of the latter is limited; the Nicoya Peninsula configuration enables a much more detailed comparison.

3. Data and Method

3.1. Hypocenter Relocation

[9] An accurate hypocenter is important for finite-fault inversions as it influences the faulting kinematics. For most large earthquakes, near-field or regional recordings are not available, so the hypocenter reported by the USGS is

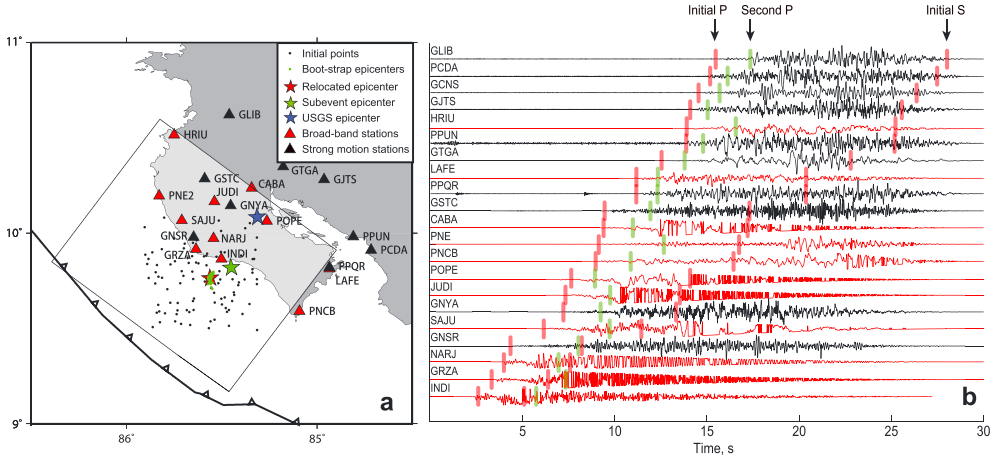

Figure 2. (a) The relocated epicenter of the 2012 Nicoya, Costa Rica event based on local seismic observations is indicated with a red-filled star, and the USGS epicenter from teleseismic data is marked with a blue-filled star. The epicenter of a strong-onset subevent in the local data is indicated with a green-filled star. Initial positions of each assumed hypocenter used in the location process are indicated by black dots to indicate the inversion stability. Hypocenters located by 40 boot-strap realizations are plotted with green-filled circles to evaluate relocation uncertainty. Local seismic stations are marked by red and black triangles for broadband and strong ground motion stations, respectively. The Middle America Trench is indicated by the barbed curve, and the rupture model area is marked by the rectangle. (b) Vertical component records from regional broadband and strong ground motion stations are shown by red and black waveforms, respectively, ordered by epicentral distance. Predicted *P* arrival times for the hypocenter and large subevent are marked by red and green bars, respectively. Predicted *S* wave arrival times of the hypocenter are also marked by the later red bars. A linear taper was applied to each trace after the initial *P* wave motion to emphasize the initial amplitudes.

commonly used in finite-fault inversion. In the case of the 2012 Costa Rica event, the seismic stations on the Nicoya Peninsula, comprising 13 broadband seismic stations and 10 strong ground motion stations, enable a more accurate hypocenter determination (Figure 2). The broadband stations are maintained by UC Santa Cruz, Georgia Institute of Technology, and Observatorio Vulcanologico y Sismologico de Costa Roca (OVSICORI-UNA), and the strong ground motion stations are maintained and distributed by Laboratorio de Ingenieria Sismica at Universidad de Costa Rica. All broadband stations went offscale for the main shock when the large seismic waves arrived; however, the timing of initial *P* arrivals is still available for locating the initial seismic radiation.

[10] To relocate the hypocenter, we picked 21 arrival times from three component records checking for reliable initial motions. A 1-D *P* wave velocity model from a local tomography study [*Deshon et al.*, 2006] was used for ray tracing. We assume the hypocenter is located on the megathrust with geometry defined from a seismic reflection profile [*Christeson et al.*, 1999]. The same fault geometry is used in our finite-fault model parameterization (Figure 3). The along-strike and along-dip position of the hypocenter and its origin time are inverted for using a classical Newton-Gaussian inversion technique. Stations within 100 km from the preliminary hypocenter are used to guarantee that the first motions are from the Pg phases. To test dependence on the initial position, 50 relocations were performed with different initial positions within a 60 km × 60 km area, centered near the preliminary hypocenter. All inversions give relocated hypocenters within ~1 km horizontal distance, indicating a stable inversion. The preferred hypocenter is 9.76°N, 85.56°W at depth of 13.1 km below sea level, which is ~10 km off the coast. The initial time is at 14:42:04.4 UTC, 2.6 s earlier than the USGS origin time for a source depth of 35 km. The averaged absolute value of the predicted initial time residual is ~0.23 s, which is close to the error of the manually picked initial arrivals. Assuming the rays are close to horizontal and a typical *P* wave velocity of ~5 km/s, then the associated epicenter location error is approximately 1.5 km.

[11] When considering the predicted *S* wave arrivals in the near-field seismic traces, we found the broadband stations are offscale after the initial *S* arrival, but there are some secondary phases between the initial *P* and *S* arrivals (Figure 2), which are probably *P* waves from rupture subevents. A consistent secondary *P* wave arrival, stronger than the first very emergent *P* arrival, could be identified around 2–3 s after the initial motion. By picking corresponding arrival times, we located a subevent hypocenter at 9.82°N, 85.47°W, at a depth of 17.2 km on the megathrust (Figure 2a). The origin time of this subevent is 14:42:07.7 UTC. Stations with epicenter distances from 20 to 100 km are used for this location, to exclude the influence of the *S* wave energy from the hypocenter in the very close stations. We used the differential arrival time between the initial motion and the subevent *P* wave motion to make a relative relocation, given the relocated hypocenter as a reference point. The subevent locates ~12 km downdip of the hypocenter and is delayed by ~3.4 s from the initial rupture, which suggests initial downdip rupture propagation at a velocity of ~3.5 km/s. The relative relocation is not strongly influenced by the uncertainty of the reference model and is sensitive to the relative location between the hypocenter and subevent location.

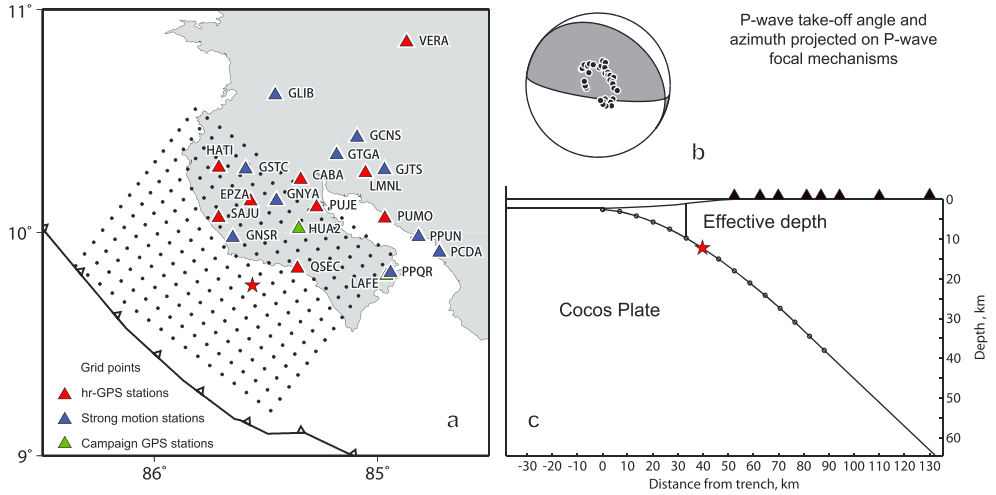

Figure 3. Rupture model parameterization. (a) Map of the rupture model grid, parameterized with 17 and 15 nodes, with 7.5 km spacing along strike and dip, respectively. The relocated epicenter is indicated by a red-filled star. The locations of local stations used in the inversion are marked by red-, blue-, and green-filled triangles for hr-GPS stations, strong ground motion stations, and lr-GPS stations respectively. (b) The azimuths and take-off angles of teleseismic *P* wave recordings used in our inversion are projected onto the lower hemisphere focal mechanism of the 2012 Nicoya, Costa Rica event. (c) Cross section indicating the fault model and ocean bottom geometry. The node depth in the flat 1-D model was taken as the effective prism thickness with dip used for each subfault preserved to correspond to the dip of the actual megathrust.

The arrival time picking of the subevent has more uncertainty than the initial motion, which introduces larger errors in the location and initial time. The estimated location and initial time of the subevent indicate downdip rupture propagation, which is a stable pattern that got proved in boot-strap algorithm, but may not be used to prescribe the rupture velocity precisely.

[12] In earthquake location procedures, errors are introduced by using a reference 1-D velocity model, which does not account for actual 3-D heterogeneities. Such error will tend to increase with propagation distance. For the 2012 Nicoya, Costa Rica event, we have 21 stations within 100 km epicentral distance and four stations within 30 km epicentral distance. For these data, reference model error that accumulates with distance will be small. To test the inversion stability, we adopted a boot-strap algorithm, in which we randomly selected half the stations for relocation in each boot-strap realization. Forty boot-strap realizations are made; the location results fall within 5 km from the preferred hypocenter location, suggesting a maximum location error of 5 km (Figure 2). The boot-strap algorithm samples different stations in each realization, varying the effects of 3-D heterogeneity. The relatively concentrated location of the boot-strap results, with standard deviation of 1.4 km and maximum of 5 km, indicates that 3-D heterogeneity does not impact our location significantly.

[13] Another concern about the location uncertainty comes from the one-sided station distribution, in which the origin time trades-off with the offshore distance of the epicenter. In our tests, location excluding the four closest stations moves the epicenter 5 km closer to the coast line and delays the initial time by ~0.5 s. This is consistent with the boot-strap location uncertainties. We use the location from the complete data set as our final hypocenter.

[14] Considering the weak amplitude of the initial local *P* wave motion, which may not be observable in the teleseismic records, it is unclear exactly what feature in the near-field signals corresponds to the teleseismic first motions (the teleseismic waves also have weak initial motions in the first few seconds). It seems likely that the USGS location has substantial uncertainty due to both the emergent onset of the *P* wave radiation during the first few seconds of this event and due to possible biases by slab heterogeneity for paths to North American and European stations. We will use the locally determined hypocenter in the finite-fault modeling as it is well constrained and compatible with the near-field ground deformations.

3.2. Fault Parameterization

[15] For the finite-fault inversion, the fault plane is parameterized with 17 and 15 subfaults along strike (307°) and dip, respectively, with 7.5 km spacing (Figure 3a). The total fault model area is 128 × 113 km^2. The 2-D fault geometry is the same as that used in the hypocenter relocation [*Christeson et al.*, 1999], with the ocean bathymetry removed and the offshore subfault depth in the flat 1-D model taken as the effective prism thickness with the depth-varying dip for each subfault preserved to correspond to the dip of the actual megathrust (Figure 3c). We adopt a multitime window inversion [*Hartzell and Heaton*, 1983], in which the source time function of each subfault is parameterized with eight symmetric triangles with 2 s rise times and 2 s shifts, which allow up to a 18 s long source time function for each subfault. We use two components of the slip vector to parameterize a rake-varying slip on each subfault and apply a nonnegative least square inversion [*Lawson and Hanson*, 1974], in which the rake of each subfault is allowed to vary between 45°

and 135°. We apply a Laplacian regularization [*Hartzell and Heaton*, 1983], which constrains the second-order gradient for each parameter to be zero.

3.3. High-Rate GPS Signals

[16] We obtained three component ground motion solutions for nine high-rate (five sps) GPS stations, which are maintained by the University of South Florida and OVSICORI-UNA and distributed by UNAVCO (Figure 3a). The high-rate positions were processed using single station bias fixing [*Bertiger et al.*, 2010] and point-positioning [*Zumberge et al.*, 1997] with the GIPSY-OASIS software of Jet Propulsion Laboratory (JPL), Pasadena, California. For these rapid deformations, the station position is estimated as a stochastic parameter, and we use high-rate (30 s) satellite clock and orbit files provided by JPL [*Desai et al.*, 2011]. The tropospheric parameters are fixed to the values estimated from a prior processing run where the positions are held fixed. The estimated standard deviation for these GPS signals is ~1.6 cm. These random errors are only a few percent of the characteristic peak displacements (~60 cm) for the 2012 Nicoya, Costa Rica event, which is small relative to uncertainties related to model parameters for our inversions. Separate processing of the data using GIPSY and GAMIT algorithms gives only a few percent differences in time series.

[17] To model the near-field ground displacements recorded by hr-GPS, Green functions for the full dynamic and static elastic deformation field must be used. For modeling hr-GPS data for the 2011 Tohoku earthquake, we used Green functions calculated by summing all normal modes up to 80 mHz for the PREM velocity structure. Those Green functions are reliable for long period ($>$ 20 s) signals and epicentral distances larger than 100 km [*Yue and Lay*, 2011, 2013]. However, for the Nicoya, Costa Rica event, we have observations at epicentral distances less than 50 km from many of the subfaults with stable signals down to periods of a few seconds. To exploit the short-period information for very near-field displacements, we applied a frequency-wavenumber (F-K) integration method including all near-field terms (Computer Programs in Seismology, Robert Herrmann). The F-K method accounts for both dynamic and static near-field ground displacements, and its static displacement predictions agree well with analytical results, such as the half-space Okada model [*Okada*, 1992]. The same 1-D velocity model used in the hypocenter relocation is used in the F-K integration. The model parameters are listed in supporting information.

[18] We calculated a dense Green function database for epicentral distances of 0–500 km and source depths of 0–50 km with 1 km increment for distance and depth. We use the nearest Green functions for each source grid node for each station, incurring minor errors ($<$0.5 km) in propagation distance, which are insignificant compared to the model grid spacing of 6 km. In our inversion for all datasets, the Green functions of each node are convolved with the subfault source time functions, and both Green functions and data are low-pass filtered at a corner frequency of 0.2 Hz, to eliminate any short-period multipathing artifacts in the data processing and any short-period propagation effects not accounted for by the 1-D velocity structure. The Green functions and hr-GPS data are down-sampled to 1 sps after low-pass filtering. Each trace has an 80 s long time window, starting at the origin time of the relocated hypocenter.

3.4. Low-Rate GPS Signals

[19] Two GPS stations on Nicoya Peninsula, HUA2 and LAFE (Figure 3), record low-rate data only (1 sample per 15 s). These two stations are located above the downdip edge of the megathrust, where there are no hr-GPS stations. Although dynamic rupture process information is not provided by the lr-GPS records, the coseismic static displacement are useful and help to constrain the slip in the southeastern region of the fault plane. The values may be affected somewhat by any afterslip occurring during the time window of the solutions. We model these static offsets using the same Green function database as used in the hr-GPS inversion, by considering only the static offset after the time-varying motions have passed. For a joint inversion, the static displacements only contribute to the accumulated seismic moment and its spatial distribution, with time-varying rupture expansion information controlled by the dynamic signals of hr-GPS and seismic recordings.

3.5. Strong Ground Motion Records

[20] The 2012 Nicoya, Costa Rica event was recorded by ~40 accelerometers across Costa Rica, out of which 10 were located within 100 km from the hypocenter (Figure 3a). These strong ground motion sensors have a flat instrument response to ground acceleration from 0.1 Hz to 40 Hz, with a sample rate of 200 sps. The lower frequency response of the strong motion sensors is not well resolved. To minimize accumulated scattering effects over long propagation distances, we only used the stations within 100 km epicentral distance for inversion. To model the strong ground motion data, we use the same Green function dataset as used for modeling the hr-GPS data. The 1-D model is not expected to be valid for periods shorter than a few seconds, so we utilize only the low-frequency portion of the acceleration recordings. Double integration of the data to ground displacement was not very stable, so we use integrations to ground velocity in the inversion. Three component ground accelerations from the 10 stations were demeaned, detrended, tapered, and integrated to ground velocity. The Green functions were differentiated to ground velocities. A band-pass filter with corner frequencies of 0.1 to 0.3 Hz was applied to limit the signals to the range of validity of the 1-D velocity model and the data. All strong motion records were cut with a 80 s long time window, starting at the origin time of the relocated hypocenter.

3.6. Teleseismic Records

[21] To ensure compatibility of the near-field source model and teleseismic observations, we include high-quality *P* wave observations in the joint inversion for a finite-fault model. The teleseismic *P* wave dataset is comprised of 33 broadband ground displacements from stations of the Federation of Digital Seismic Networks (FDSN), accessed through the Incorporated Research Institutions for Seismology (IRIS) data center. The data were selected from hundreds of available FDSN seismograms to have good azimuthal coverage (Figure 3b) and high signal-to-noise ratios, for epicentral distances from 40° to 90°. Instrument responses were removed to reconstitute ground displacement with a band-pass filter with corner frequencies of 0.005 to 0.9 Hz. A 90 s long time window was extracted from the raw data, starting 10 s prior

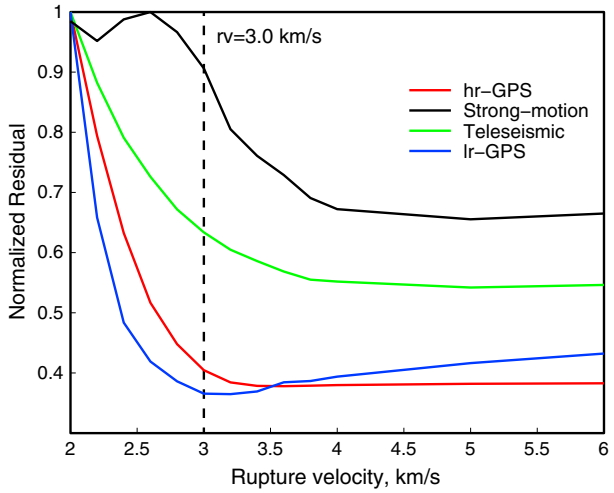

Figure 4. Trade-off curves indicating normalized inversion residual versus rupture velocity for each dataset. Red, black, green, and blue curves indicate hr-GPS, strong ground motion, lr-GPS, and teleseismic datasets, respectively. Joint inversions were made using constant rupture velocities varying from 2 km/s to 6 km/s. A rupture velocity of 3.0 km/s was used for the final preferred model.

to the clearest first arrival of the *P* waves. Unlike the near-field data, which use absolute time, the arrival times of teleseismic waves are influenced by remote path structures, and in our inversion, the *P* wave initial motions were aligned manually. The teleseismic *P* waves have emergent initial arrivals, consistent with what we observed in the near-field data. The ambiguous initial arrivals raise some uncertainty of how to align the teleseismic dataset with the locate dataset that uses absolute time. Considering it likely that the very weak initial *P* waves from the hypocenter seen in the near-field data are missed from the teleseismic *P* wave onsets, we assume that the teleseismic initial motion is actually associated with the strong subevent ~3 s after the hypocentral time. To align with the absolute time of the local data, the aligned teleseismic *P* wave records were shifted by 3 s. Such a shifted alignment is suggested by inversion results when the teleseismic data are given very small weight and the inversion is mainly controlled by the local hr-GPS data. Those inversions produce uniform delays in the teleseismic data fitting when the teleseismic dataset is aligned with the rupture initial. Inversions with a 3 s alignment shift match the early portions of both local and teleseismic data. The teleseismic Green functions are generated with a reflectivity method which accounts for interaction in 1-D layered structures on both the source and receiver sides [*Kikuchi et al.*, 1993]. The local 1-D layered model is used for the source side, and a typical continental model is used for the receiver side. The same band-pass filter used for the data is applied to the Green functions.

3.7. Weighting Between Datasets

[22] Joint inversions always present challenges in relative weighting between different datasets. In our joint inversion, we are combining near-field displacement field, velocity field, and teleseismic displacement field in one joint inversion, for which the optimal relative weighting is hard to determine quantitatively. Our choice of weighting between datasets comes from evaluation of attributes of the different datasets. In our joint inversion, the most reliable information comes from the hr-GPS observations, which provides stable ground displacement information that covers a wide frequency band. Teleseismic P and SH data have limited spatial resolution due to high apparent velocities and are down-weighted in the joint inversion. Regional strong ground motion data suffer from unknown receiver structure, in which the sediment effect can be significant. Also, we invert ground velocities, which involves error introduced by data integration and Green's function differentiation. The band pass spanned by the strong ground motion data is also limited at low frequency, so the weighting given to the strong ground motions is the lowest. Our preferred weighting between hr-GPS lr-GPS/teleseismic/strong ground motion data are 1/0.2/0.1 after normalization by the mean data value and sample points. We explored ranges of relative weights finding stable results for moderate deviations about these preferred choices.

4. Results and Discussion

4.1. Rupture Velocity

[23] In linear finite-fault model inversions, rupture velocity plays an important role in the kinematic expansion and accumulation of slip. Teleseismic *P* wave data have limited resolution of rupture velocity, and it is often necessary to draw upon constraints from other methods, such as backprojections, and to allow relatively long subfault rupture durations to avoid imposing a tight expanding rupture annulus [*Lay et al.*, 2010]. However, well-distributed near-field data, particularly hr-GPS data, exhibit less sensitivity to the initial rupture velocity because they have intrinsic sensitivity to the spatial slip distribution [*Yue and Lay*, 2011, 2013]. With the constraints from both static displacement and dynamic waveform fitting, inversions with hr-GPS tend to yield stable rupture models as long as the input rupture velocity is high enough to capture the real rupture front and the source time duration is long enough to cover the whole rupture duration. Although the basic rupture model from hr-GPS inversion will not be greatly impacted by the input rupture velocity, the data-misfit residual will be partially influenced by the rupture velocity. If the rupture velocity is less than the real rupture velocity, the initial motion in the data may not be well modeled although the static displacements may be well fit; if the rupture velocity is at least as high as the real rupture velocity, we do not expect significant waveform misfit residual for increasing rupture velocity. We can exploit the trade-off curve of rupture velocity and waveform misfit residual to define an appropriate model rupture velocity.

[24] Trade-off curves of rupture velocity versus normalized waveform mismatch residual, for joint inversions with constant rupture velocity ranging from 2.0 km/s to 6.0 km/s, are shown in Figure 4. A rupture velocity of 3.0 km/s gives a turning point in the trade-off curve for hr-GPS data, suggesting that it is a sufficiently high rupture velocity to account for the data onsets. In our joint inversions, the rupture space-time pattern is mainly controlled by the hr-GPS data because they provide the best resolution with the maximum weighting, the teleseismic data and strong ground motion data contributing to details of the slip expansion, constrained to the model space compatible with the hr-GPS signals. A rupture velocity of 3.0 km/s also gives a minimum residual

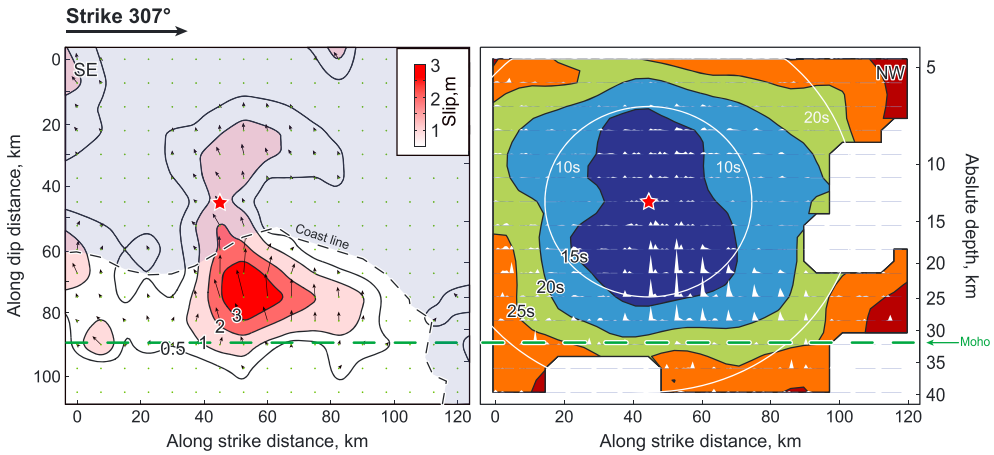

Figure 5. (a) Rupture-plane view of the slip distribution for our preferred model with a rupture velocity of 3.0 km/s. The absolute depths of the nodes for the varying-dip model are shown on the right. The maximum slip is ~4.4 m located near the center of the main slip patch at around 25 km depth. The total seismic moment is 3.51×10^{20} Nm, which gives an M =7.63 earthquake. The hypocenter on the fault plane is marked with a red-filled star. Only nodes with a slip larger than 0.5 m are contoured, and the slip directions at each node are indicated with black arrows. The coastline is marked by the dashed curve with the offshore region shaded blue. The Moho interface at ~32 km depth is projected onto the fault plane and indicated with a dashed green line. (b) Source time functions of each subfault node are shown as white polygons. The centroid time of each node is contoured as the background colored map. Constant rupture velocity expansion time counters are marked as white concentric circles.

mismatch for the static lr-GPS data. Static GPS data have no resolution of rupture propagation; however, in the joint inversion, the alignment for the hr-GPS data allows all of the static signals to be matched simultaneously. The teleseismic *P* wave data show a broad residual minimum between rupture velocities of 3.5 km/s to 4.0 km/s, with only a small increase in misfit for a rupture velocity of 3.0 km/s. For the teleseismic dataset, the maximum misfit residual at rupture velocity of 2.0 km/s is no more than 2 times the minimum residual at rupture velocity of 6.0 km/s, indicating the limited teleseismic resolution of rupture velocity. The strong ground motion data have some resolution of rupture locations and rupture velocity, but higher rupture velocity is intrinsically preferred by the more distant short-period strong ground motion data because it allows for a larger rupture front and more associated inversion parameters to try to fit the data complexity. The trade-off curve for strong ground motion data suggests a preferred rupture velocity between 3.5 km/s and 4.0 km/s, which is similar to that for the teleseismic dataset. Overall, the behavior for the hr-GPS data leads us to prefer models using a rupture velocity of 3.0 km/s, but we include relatively long subfault source time functions to ensure that the final model is not excessively controlled by the imposed rupture kinematics.

4.2. Preferred Rupture Model

[25] The slip distribution, subfault source time functions, and space-time rupture evolution of our preferred model are shown in Figure 5. The overall rupture propagation direction is from updip to downdip, which is consistent with the relative locations between the relocated hypocenter and the 3 s later subevent. The main large slip patch locates beneath the peninsula, spanning ~30 km along dip and ~70 km along strike. The average slip of the well-resolved primary slip region (slip > 1m) is ~2 m, indicating an average static stress drop of ~3 MPa. The total seismic moment of our preferred model is 3.5×10^{20} Nm, which gives $M_w = 7.6$. The peak slip amplitude in the model is ~4.4 m, located downdip from the hypocenter. The centroid depth of the slip distribution is ~21 km, which is shallower than the GCMT centroid (30 km) and W-phase centroid estimates (30 to 40km). The centroid location is at 9.91°N and 85.54°W, which is ~14 km to the north of the GCMT centroid location and ~44 km to the west of the W-phase centroid location. The dominant slip direction is at 90° rake, with minor right-lateral component, which is consistent with the 118° rake of the GCMT solution, as well as the slightly oblique subduction direction.

[26] There is a secondary slip patch located updip offshore and to the north-west of the hypocenter, which is a stable feature of many inversions we conducted. However, the moment of this offshore rupture patch is approximately 13% of the total moment, and the waveform contributions from this patch are too weak to be confidently isolated in the various data signals. The seismic moment of the updip slip patch is $\sim 4.5 \times 10^{19}$ Nm, corresponding to an M_w 7.0 earthquake. Because of its offshore location, it is difficult to constrain the precise moment (and existence) of this secondary slip patch and the moment and location of such a patch varies with different selection of inversion parameters, but there is some increase in waveform mismatch if we truncate the offshore grid, so it appears to be a minor part of the coseismic rupture.

[27] For the main slip patch beneath the Nicoya peninsula, the source time duration is ~10 s for most subfaults, with a sharp initial energy release and slow decay. Such a moment rate shape is consistent with a crack model. Secondary pulses or multiple peaks are present on a few subfaults, which may present repeated slip events or effects of our regularization. For FFM inversion, such details are not usually very stable.

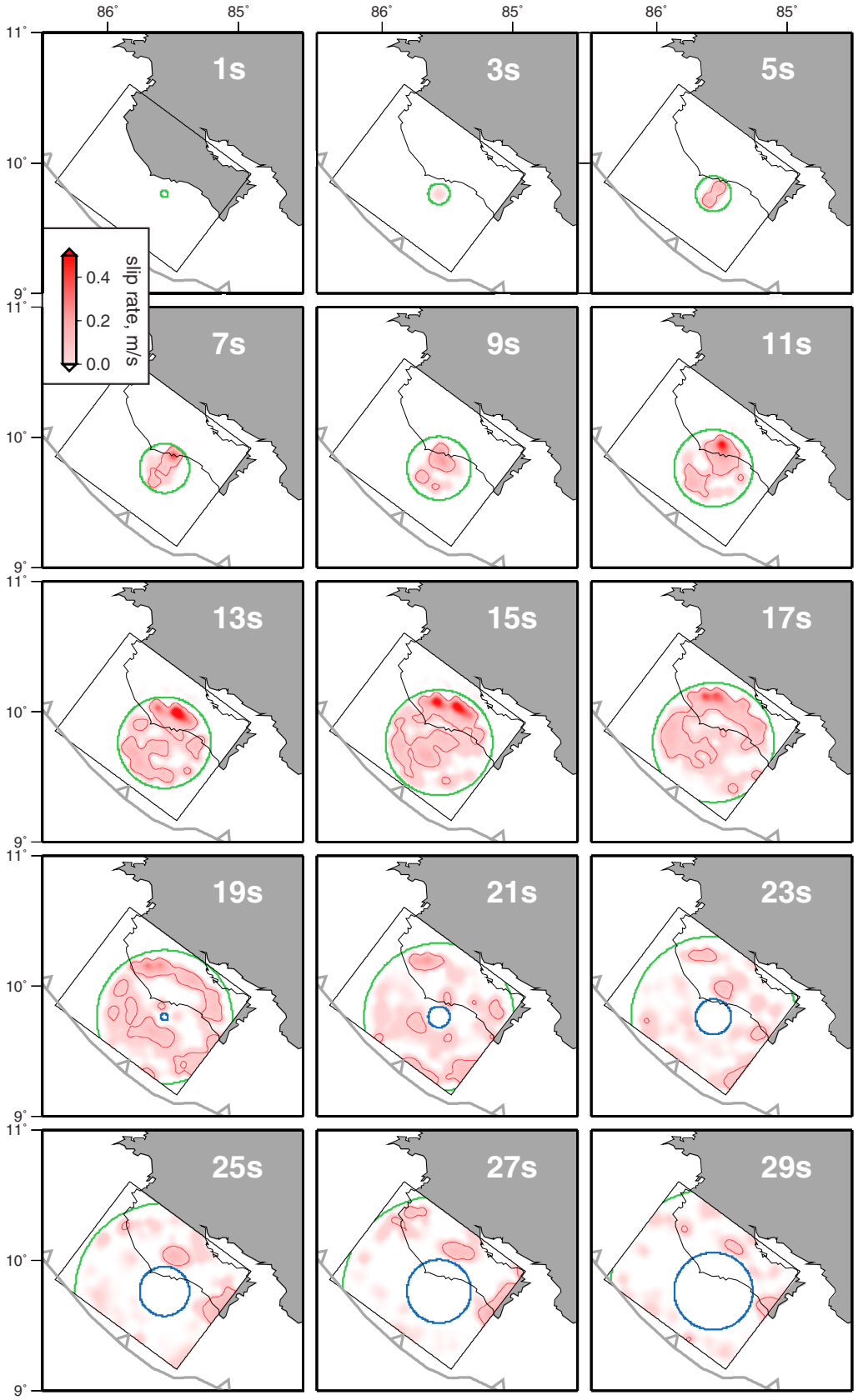

Figure 6. Snapshots of the space-time history of slip velocity during the 2012 Nicoya, Costa Rica earthquake for our preferred rupture model are shown in 2 s intervals. Particle motion velocity is shown with a red scale. The kinematic expanding rupture annulus is indicated by the green (rupture front) and blue (healing front) circles.

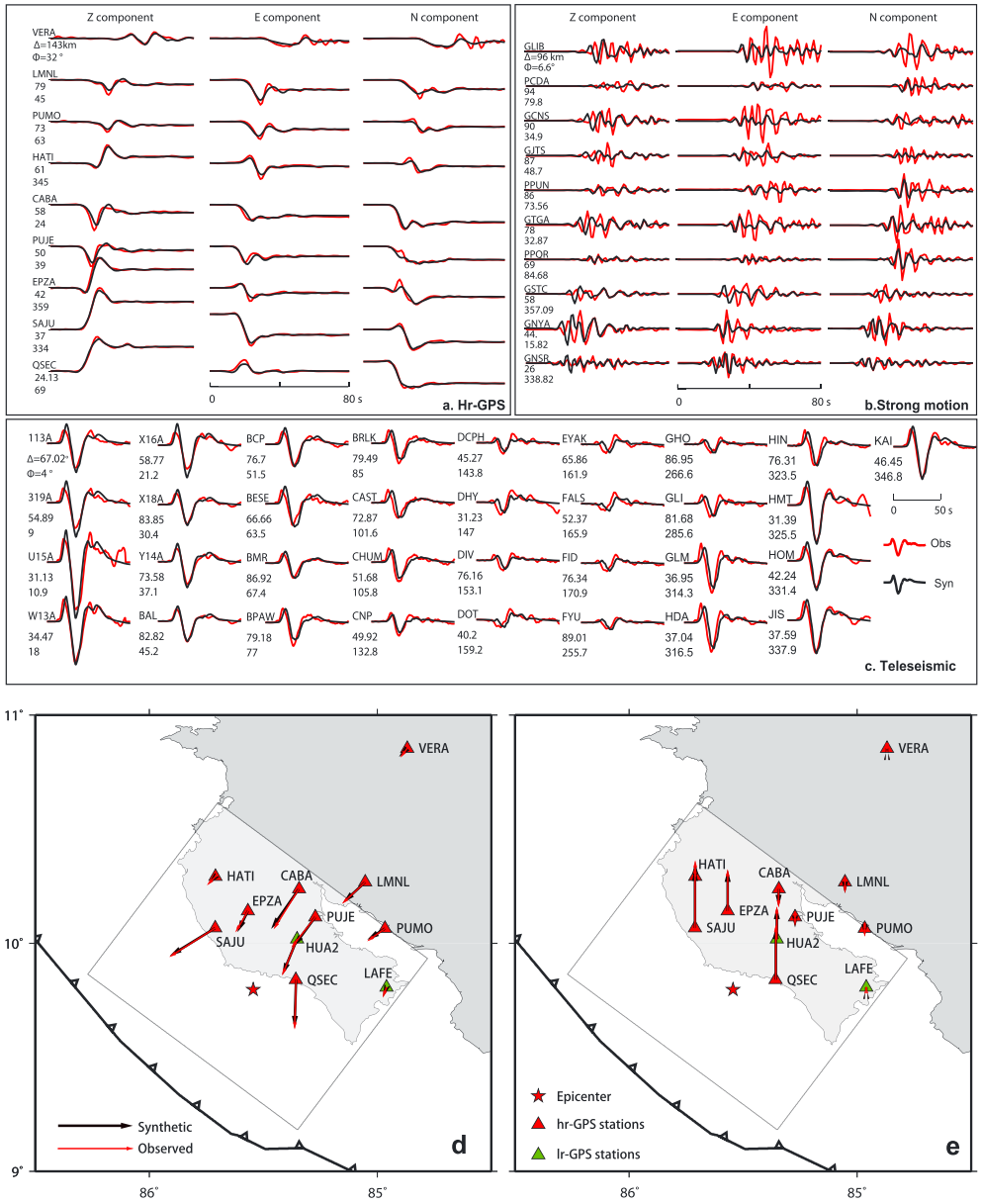

Figure 7. Observed (red) and modeled (black) waveforms for (a) hr-GPS, (b) strong ground motion, and (c) teleseismic *P* wave data for the preferred joint inversion. Three-component hr-GPS and strong ground motion records and vertical teleseismic *P* wave records are used in the inversion. Hr-GPS and strong ground motion are ordered by epicentral distance; teleseismic *P* wave data are ordered by azimuth. Station names, epicentral distances, and azimuths are shown by each trace. Observed and modeled coseismic static displacements for nine hr-GPS stations and two lr-GPS stations are plotted with red and black arrows, respectively, for (d) horizontal motions and (e) vertical motions. Stations locations of hr-GPS and lr-GPS stations are plotted with red- and green-filled triangles, respectively.

Given the uncertainty in the Green's functions, we do not try to interpret all of the subfault complexity, noting that the basic pattern is quite uniform and simple.

[28] The rupture evolution is most clearly depicted with snapshots of the space-time history of slip velocity (Figure 6). The rupture initiated near the hypocenter and expanded updip and downdip slowly within 5 s; the main slip patch started to rupture at 7 s and continuously propagated downdip. At 15 s, the main rupture front reached its downdip limit and began to extend bilaterally along strike, with the north-west propagation dominating. Around 15–17 s, the rupture reached its peak moment release, which covers a length of ~60 km along strike. The slip of the main rupture area ended at ~21 s. The rupture of the isolated updip slip patch starts at 11 s and lasts to 19 s, giving a subsource duration of 8 s. Finite-fault model details are provided in the supporting information.

4.3. Data Fits

[29] The waveform and static displacement fits of all datasets are shown in Figures 7a–7e. Generally for finite-fault

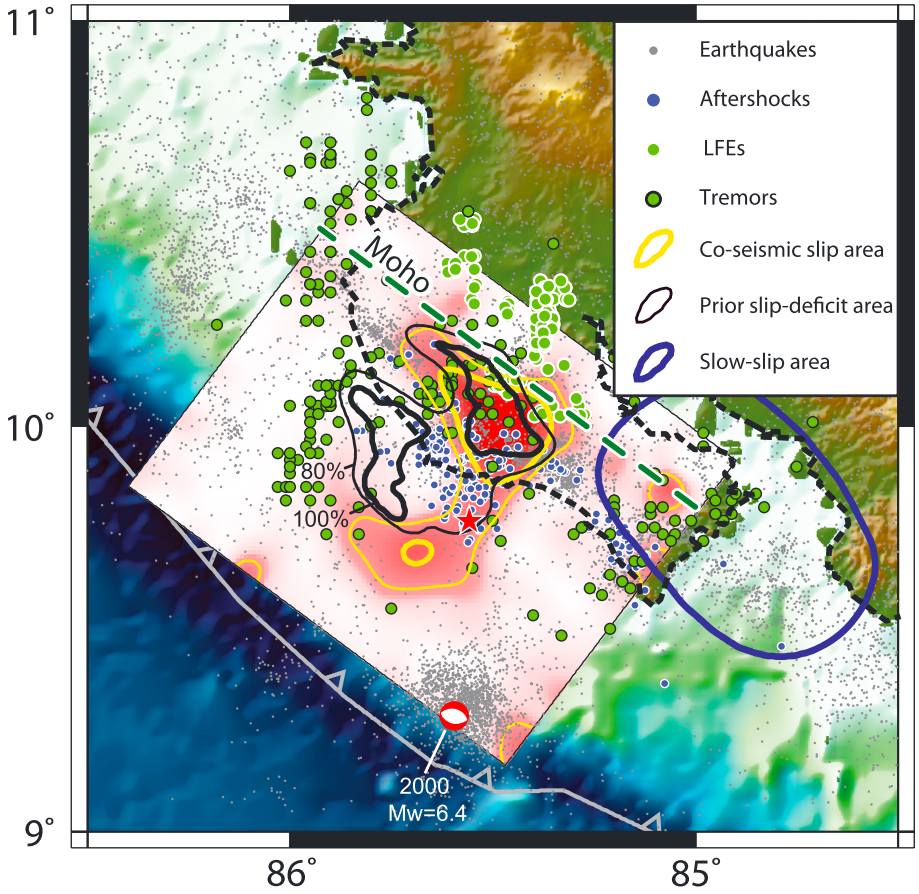

Figure 8. Summary map of the 2012 Nicoya, Costa Rica rupture model and surrounding fault zone observations. The coseismic slip distribution for our preferred rupture model is mapped with red-white color scale, with regions of coseismic slip > 1.2 m outlined in thin yellow and slip > 2.0 m outlined with thick yellow. The epicenter is shown with a red star. The interseismic locked region is outlined in thick/thin black counters for > 80% and 100% slip deficit [*Feng et al.*, 2012], respectively. The slip area (slip > 70 mm) of the 2007 slow slip event [*Outerbridge et al.*, 2010] is outlined in blue. Well-located background seismicity is plotted with grey-filled circles. About 10,000 of these events are from 1999 to 2001 [*Ghosh et al.*, 2008], ~1500 events from 2007, and 4800 events from 2009. Preliminary aftershocks within a month of the 2012 main shock are plotted with blue-filled circles. Low-frequency earthquakes (LFE) identified within tremor on 17 May 2007 [*Brown et al.*, 2009] are plotted with green-filled, white-bordered circles. Tremor events from May 2007, August 2008, and April 2009 are plotted with green-filled, black-bordered circles [*Walter et al.*, 2011]. The intersection between the fault plane and the overriding plate Moho interface are project in the map as a green dashed line.

inversions, the quality of waveform fits depends on the fault parameterization, Green's function adequacy, and inversion regularization. It always presents a challenge to optimize the model parameters and waveform mismatch residuals. This is particularly true for waveform fits in joint inversions because how the residuals distribute across different datasets strongly depends on the relative weighting used. Because the relative weighting between GPS/teleseismic/strong ground motion data is 1/0.2/0.1, the inversion tends to fit the data in order from highly weighted to lowly weighted datasets. Thus, the GPS data are best fit in our joint inversion, and the strong ground motion data are least fit.

[30] Figure 7 demonstrates that both static displacements and dynamic waves are well fit for the hr-GPS dataset (Figures 7a, 7d, and 7e) and lr-GPS data (Figures 7d and 7e). The teleseismic datasets are satisfactorily modeled including the first peak, indicating acceptable time coordination with the local absolute time signals. The strong ground motion data are generally matched in phase, but the amplitudes of larger arrivals at several stations are underestimated. Stations with significantly underpredicted waveforms, such as GTGA and GCNS, are at locations which are described to be "very soft" in their logging information; consequently, sediment amplification effects may be significant. Overall, this joint inversion achieved good waveform fits to the various datasets, which suggests that the inversion model is a reasonable first-order representation of the broadband source. As with all such finite-fault models, it is challenging to prescribe uncertainties, and as we proceed to compare the model with other observations, we will

emphasize those aspects of the model that are most stable for a wide range of permutations of data sets, relative weights, rupture velocity, and other model parameters.

4.4. Comparison With Other Megathrust Deformation Observations

[31] Figure 8 compares our preferred slip model for the 2012 Nicoya, Costa Rica event with other characterizations of megathrust deformation around the Nicoya Peninsula. The interseismic locking pattern inverted by *Feng et al*. [2012] using the daily solution of continuous and campaign GPS data with an averaged time span of ~8 years has an extended pattern below both land and ocean areas. In their results, two locked patches are resolved, with one located updip offshore and the other located inland (black outlines in Figure 8), separated by ~30 km, and embedded within a larger region of at least 80% locking. The downdip slip-deficit patch is consistent with the coseismic rupture area having slip amplitude larger than 2 m in the 2012 event. The average slip amount in this area is ~3 m. For an average plate convergence rate of 78 mm/yr [*Protti et al*., 2012] and a forearc motion rate of 10 mm/yr [*LaFemina et al*., 2009], the projected slip accumulation rate in the trench-normal direction is ~77 mm/yr. Thus, ~3 m average slip released in this region could have accumulated over ~40 year, which is compatible, given the uncertainties, with the ~60 years since the 1950 rupture under the Nicoya Peninsula.

[32] If the slip distribution were known for the 1950 and 1900 events, then a slip versus time interval analysis could provide insight into the interseismic cycle beneath the Nicoya peninsula [*Shimazaki and Nakata*, 1980]; however, there is no knowledge of the slip distributions for the 1950 and 1900 events, apart from their estimated magnitude and general location (Figure 1). Any estimation of slip amount for these two older events requires assumptions about stress drop or rupture scale, as well as location of the slip.

[33] The offshore locked patch does not colocate with the offshore slip patch in the rupture model. Given that the coseismic slip and interseismic slip-deficit inversions both have limited offshore resolution, the regions could coincide, but the amount of slip is certainly less than that of the patch below land. If the interseismic slip-deficit estimation is reliable in *Feng et al*. [2012], there should still be substantial strain accumulated offshore. If we assume the 1950 $M = 7.8$ event ruptured both the updip and downdip locked patches rather than only the downdip one, a comparable amount of slip accumulation to that released in 2012 may exist offshore and a similar size earthquake may occur in the future.

[34] Aftershock locations [*Newman et al*., 2013] within 5 km from the megathrust are also shown in Figure 8, with most surrounding the main downdip rupture patch and only a few locating within the region with 2 m or larger slip. Many aftershocks are found in the region with >80% locking and low levels of coseismic slip. These aftershock locations will likely be improved by manual adjustment of *P* and *S* wave arrival times and relocation in a 3-D velocity model, but it is notable that the offshore high slip-deficit region has very few aftershocks in it. If it is correctly placed, it is plausible that this patch remains unbroken and may fail in the future in an earthquake comparable in size to the 2012 event.

[35] Nonvolcanic tremor events around Nicoya have been detected offshore as well as downdip on the megathrust [*Walter et al*., 2011]. Tremor location estimates are distributed on both sides along strike and downdip of the coseismic slip patch (Figure 8). A few tremor events overlap the main coseismic slip patch, which gives some possibility that tremor may colocate with the coseismic rupture area or be on parallel faults. It is important to recognize that *Walter et al*. [2011] used an envelope cross-correlation method to locate the tremor events, which may have significant location uncertainties, especially for offshore events. In general, the tremor event distribution is adjacent to the coseismic slip area and the interseismic locked areas. Tremor relocations using more advanced methods are being pursued to enable detailed comparison with the coseismic slip distribution. It is also interesting that the tremor events colocate with the areas that show relatively high b values ($b \sim 2.0$) in background seismicity both northwest and southeast of the Nicoya Peninsula interpreted as relatively weak seismic coupling [*Ghosh et al*., 2008]. The main coseismic area ruptured during the 2012 Nicoya, Costa Rica event has an ordinary b-value ($b \sim 1.0$) in background seismicity. In 2007, a slow slip event [*Outerbridge et al*., 2010] occurred southeast of the main slip patch in a region with seismic tremor that is relatively deep on the megathrust. This region may be downdip of the 1990 earthquake rupture zone (Figure 1). There were few aftershocks in this region, and almost no coseismic slip is imaged there.

[36] Low-frequency earthquakes accompanying the 2007 slow slip event were located precisely by a template matching technique [*Brown et al*., 2009] and locate downdip of the 2012 coseismic slip region. The downdip limit of large coseismic slip is near depths of 30 to 35 km, with a large slip gradient of 0.25 m/km, in contrast with the updip slip gradient of ~0.1 m/km (Figure 5a). The large slip gradient may be related to an abrupt material property change near 30–35 km depth. The Moho boundary in the overriding plate intersects with the subducting plate at a depth of ~32 km [*Deshon et al*., 2006], which may provide such a material property change near the slip zone margin. It has been suggested that the mantle wedge beneath Costa Rica is 15–25% serpentinized [*DeShon and Schwartz*, 2004; *DeShon et al*., 2006] as a result of fluid release from the subducting plate. A transition from mafic granulite lower crust to serpentinized mantle will lead to frictional transition from unstable sliding to stable-sliding, with low-frequency earthquakes possibly indicating such a transition zone. Our rupture model suggests that the slip-deficit patch and coseismic slip zone only extend to the bottom of the upper plate lower crust, with the deeper megathrust strain releasing as ductile deformation with low-frequency earthquakes.

[37] Figure 8 reveals a complex intermingling of different megathrust deformation processes rather than a simple depth-varying segmentation between stable sliding and unstable sliding domains. The correspondence between the region of large slip deficit and the coseismic slip in the 2012 event is particularly striking. Such a pattern is not unexpected, but this may be the best-resolved correlation for any megathrust due to the fortuitous land distribution provided by the Nicoya Peninsula. The apparent lack of large slip in the offshore locked patch raises the possibility of a comparable earthquake to rupture that region in the future. It is interesting that both the slip-deficit and coseismic slip regions are surrounded by lateral and updip and downdip transitions to regions of slow

slip, tremor, and/or low-frequency earthquakes. The lateral transition from strain accumulation/coseismic rupture in the northwest to slow slip and tremor in the southeast coincides with the change in underthrust Cocos plate crustal origin and the along-strike gradients in thermal structure of the subducting plate. The moderate scale length of the locked patches and coseismic slip zone may be related to absence of much larger earthquakes in this seismically active region, as appears to be the case along much of the Middle American trench [e.g., *Ye et al*., 2013]. The existence of plate boundary parallel deformation of the fore arc, which increases toward the north along Nicaragua and El Salvador [e.g., *LaFemina et al*., 2009], may also play a role in constraining the lateral continuity of strongly locked regions on this megathrust.

[38] The observation of shallow tremor offshore of northwestern Nicoya Peninsula is a distinctive attribute of this megathrust. This appears to be outside of the large slip-deficit regions and coseismic slip area. The very shallow megathrust appears to have ruptured to the northwest in the 1992 Nicaragua tsunami earthquake, and the possibility of an updip rupture extending to the trench offshore of the Nicoya Peninsula should be considered. The 2012 coseismic slip did not appear to drive much slip offshore, other than the one patch discussed above, but it is possible that the unruptured slip-deficit region may have prevented rupture from extending into the shallow part of the wedge. The 2011 Tohoku earthquake demonstrated that with a large enough downdip rupture of a locked patch, it is possible to drive slip all the way to the trench, but the frequent failure of a modest size locked region under the Nicoya Peninsula may reduce the likelihood of such a compound rupture in this region. The 2010 Mentawai tsunami earthquake ruptured updip of larger megathrust events in 2007, so it is difficult to rule out occurrence of a rare tsunami earthquake in the shallow region of the Nicoya megathrust.

[39] The regional occurrence of low-frequency earthquakes, seismic tremor and slow slip events, adjacent to the area of large coseismic slip confirms prior studies indicating that the Costa Rica megathrust has very diverse frictional properties [e.g., *Schwartz and Rokosky*, 2007; *Walter et al*., 2011], which may be related to variations in sediment composition, temperature distribution, and fluid content. In the subduction zone beneath the Nicoya Peninsula, each region of the megathrust appears to have a preferred strain release mechanism, and further work is needed to constrain the total deformation budget of each process to evaluate how the overall plate convergence is being accommodated.

5. Conclusion

[40] Using extensive near-field observations, comprising hr-GPS, lr-GPS, and strong ground motion data, together with teleseismic *P* wave observations in a joint inversion, we obtained a detailed and stable space-time slip model for the 5 September 2012 Nicoya, Costa Rica earthquake. The relocated hypocenter location is found to be 9.76°N, 85.56°W at depth of 13.1 km below sea level and ~10 km off the coast. The initial time is at 14:42:04.4 UTC, 2.6 s earlier than the USGS origin time for a source depth of 35 km. A strong subevent is located at 9.82°N, 85.47°W, at a depth of 17.2 km on the megathrust, with an initial time of 14:42:07.8, and may correspond to the detectable first-arrival teleseismically. The coseismic rupture extends from the hypocenter downdip with a total source duration of ~21 s, at an average rupture velocity of 3.0 km/s. The area of large slip spans ~30 km along dip and ~70 km along strike, with maximum slip of 4.4 m. The total seismic moment is 3.5×10^{20} Nm, which gives $M_w = 7.6$.

[41] The area of large coseismic slip correlates well with a previously determined on shore region of 100% interseismic slip deficit or locking, with full release of strain accumulation over ~40 years. A small region offshore appears to have coseismically ruptured with the equivalent of an M_w 7.0 earthquake. This slip locates adjacent to the updip 100% locked patch and may have only released a small amount of the accumulated interseismic strain. This updip region appears to have the potential to rupture in the future with a magnitude comparable to the 2012 Nicoya, Costa Rica event. The main shock slip patch is surrounded by aftershock activity, nonvolcanic tremor events, low-frequency earthquakes, and slow slip events. This confirms previous studies suggesting that the Costa Rica megathrust has very diverse frictional properties that are not simply depth dependent but also vary along strike. This may be related to variations in sediment composition, temperature distribution, and fluid content. Each region of the megathrust appears to have a preferred strain release mechanism.

[42] **Acknowledgments.** We made extensive use of the frequency-wavenumber integration code in the seismic wave simulation software made openly available by Robert Herrmann (http://www.eas.slu.edu/eqc/eqccps.html). We thank Víctor González for installing and operating the Nicoya seismic and CGPS networks, and Aaron Moya from LIS-UCR for providing the strong motion data. We thank two anonymous reviewers and the Associate Editor for their helpful reviews. This work made use of GMT and SAC software. The IRIS DMS data center was used to access the seismic data from Global Seismic Network and Federation of Digital Seismic Network stations. This work was supported by NSF grants EAR-1245717 (T.L.) and OCE-0841061 and EAR-0842338 (S.Y.S). We thank Jake Walter for providing the aftershock catalog.

References

Allen, T. I., K. D. Marano, P. S. Earle, and D. J. Wald (2009), PAGER-CAT: A composite earthquake catalog for calibrating global fatality models, *Seismol. Res. Lett.*, *80*, 57–62, doi:10.1785/gssrl.80.1.57.

Ammon, C. J., T. Lay, H. Kanamori, and M. Cleveland (2011), A rupture model of the 2011 off the Pacific coast of Tohoku Earthquake, *Earth Planets Space*, *63*, 693–696, doi:10.5047/eps.2011.05.015.

Audet, P., and S. Y. Schwartz (2013), Hydrologic control of forearc strength and seismicity in the Costa Rican subduction zone, *Nat. Geosci.*, *6*(10), 852–855.

Avants, M., S. Schwartz, A. Newman, and H. DeShon (2001), Large underthrusting earthquakes beneath the Nicoya Peninsula, *Eos Trans. AGU*, *82*(46), Fall Meet. Suppl., Abstract T52E-07.

Barckhausen, U., C. R. Ranero, R. von Huene, S. C. Cande, and H. A. Roeser (2001), Revised tectonic boundaries in the Cocos Plate off Costa Rica: Implications for the segmentation of the convergent margin and for plate tectonic models, *J. Geophys. Res.*, *106*(B9), 19,207–19,220, doi:10.1029/2001JB000238.

Bertiger, W., S. Desai, B. Haines, N. Harvey, A. Moore, S. Owen, and J. Weiss (2010), Single receiver phase ambiguity resolution with GPS data, *J. Geod.*, *84*(5), 327–337.

Brown, J. R., G. C. Beroza, S. Ide, K. Ohta, D. R. Shelly, S. Y. Schwartz, W. Rabbel, M. Thorwart, and H. Kao (2009), Deep low-frequency earthquakes in tremor localize to the plate interface in multiple subduction zones, *Geophys. Res. Lett.*, *36*, L19306, doi:10.1029/2009GL040027.

Christeson, G. L., K. D. McIntosh, T. H. Shipley, E. R. Flueh, and H. Goedde (1999), Structure of the Costa Rica convergent margin, offshore Nicoya Peninsula, *J. Geophys. Res.*, *104*(B11), 25,443–25,468, doi:10.1029/1999JB900251.

DeMets, C., R. G. Gordon, and D. F. Argus (2010), Geologically current plate motions, *Geophys. J. Int.*, *181*, 1–80, doi:10.1111/j.1365-246X.2009.04491.x.

Desai, S. D., W. Bertiger, B. Haines, N. Harvey, C. Sella, A. Sibthorpe, and J. P. Weiss (2011), Results from the reanalysis of global GPS data in the

IGS08 reference frame, Abstract G53B-0904 presented at 2011 Fall Meeting, AGU, San Francisco, Calif., 5–9 Dec.

DeShon, H. R., and S. Y. Schwartz (2004), Evidence for serpentinization of the forearc mantle wedge along the Nicoya Peninsula, Costa Rica, *Geophys. Res. Lett.*, *31*, L21611, doi:10.1029/2004GL021179.

DeShon, H. R., S. Y. Schwartz, A. V. Newman, V. González, M. Protti, L. M. Dorman, T. H. Dixon, D. E. Sampson, and E. R. Flueh (2006), Seismogenic zone structure beneath the Nicoya Peninsula, Costa Rica, from three-dimensional local earthquake *P*- and *S*-wave tomography, *Geophys. J. Int.*, *164*(1), 109–124, doi:10.1111/j.1365-246X.2005.02809.x.

Dixon, T. H., S. Schwartz, M. Protti, V. Gonzalez, A. Newman, and J. Marshall (2013), Detailed data available for recent Costa Rica earthquake, *EOS, Trans. Am. Geophys. Union*, *94*(2), 17–18.

Feng, L., A. V. Newman, M. Protti, V. González, Y. Jiang, and T. H. Dixon (2012), Active deformation near the Nicoya Peninsula, northwestern Costa Rica, between 1996 and 2010: Interseismic megathrust coupling, *J. Geophys. Res.*, *117*, B06407, doi:10.1029/2012JB009230.

Ghosh, A., A. V. Newman, A. M. Thomas, and G. T. Farmer (2008), Interface locking along the subduction megathrust from b-value mapping near Nicoya Peninsula, Costa Rica, *Geophys. Res. Lett.*, *35*, L01301, doi:10.1029/2007GL031617.

González-Salas, V., and J. M. Protti-Quesada (2005), Afinamiento del potencial sísmico y monitoreo de la brecha sísmica de Nicoya, no. 147, pp. 12–15.

Harris, R. N., and K. Wang (2002), Thermal models of the Middle America Trench at the Nicoya Peninsula, Costa Rica, *Geophys. Res. Lett.*, *29*(21), 2010, doi:10.1029/2002GL015406.

Hartzell, S. H., and T. H. Heaton (1983), Inversion of strong ground motion and teleseismic waveform data for the fault rupture history of the 1979 Imperial Valley, California, earthquake, *Bull. Seismol. Soc. Am.*, *73*(6A), 1553–1583.

Ihmlé, P. F. (1996), Monte Carlo slip inversion in the frequency domain: Application to the 1992 Nicaragua Slow Earthquake, *Geophys. Res. Lett.*, *23*(9), 913–916, doi:10.1111/j.1365-246X.1996.tb01536.x.

Iinuma, T., M. Protti, K. Obana, V. González, R. Van der Laat, T. Kato, S. Miyazaki, Y. Kaneda, and E. Hernández (2004), Inter-plate coupling in the Nicoya Peninsula, Costa Rica, as deduced form a trans-peninsula GPS experiment, *Earth Planet. Sci. Lett.*, *223*, 203–212, doi:10.1016/j.epsl.2004.04.016.

Ji, C., K. M. Larson, Y. Tan, K. W. Hudnut, and K. Choi (2004), Slip history of the 2003 San Simeon earthquake constrained by combining 1-Hz GPS, strong motion, and teleseismic data, *Geophys. Res. Lett.*, *31*, L17608, doi:10.1029/2004GL020448.

Jiang, Y., S. Wdowinski, T. H. Dixon, M. Hackl, M. Protti, and V. González (2012), Slow slip events in Costa Rica detected by continuous GPS observations, 2002–2011, *Geochem. Geophys. Geosyst.*, *13*, Q04006, doi:10.1029/2012GC004058.

Kanamori, H., and M. Kikuchi (1993), The 1992 Nicaragua earthquake: A slow tsunami earthquake associated with subducted sediments, *Nature*, *361*, 714–716, doi:10.1038/361714a0.

Kikuchi, M., H. Kanamori, and K. Satake (1993), Source complexity of the 1988 Armenian earthquake: Evidence for a slow after-slip event, *J. Geophys. Res.*, *98*(B9), 15,797–15,808, doi:10.1029/93JB01568.

Koketsu, K., et al. (2011), A unified source model for the 2011 Tohoku earthquake, *Earth Planet. Sci. Lett.*, *310*(3), 480–487, doi:10.1016/j.epsl.2011.09.009.

LaFemina, P., T. H. Dixon, R. Govers, E. Norabuena, H. Turner, A. Saballos, G. Mattioli, M. Protti, and W. Strauch (2009), Fore-arc motion and Cocos Ridge collision in Central America, *Geochem. Geophys. Geosyst.*, *10*, Q05S14, doi:10.1029/2008GC002181.

Lawson, C. L., and R. J. Hanson (1974), *Solving Least Squares Problems*, vol. 161, Prentice Hall, Englewood Cliffs, New Jersey.

Lay, T., C. J. Ammon, A. R. Hutko, and H. Kanamori (2010), Effects of kinematic constraints on teleseismic finite-source rupture inversions: Great Peruvian earthquakes of 23 June 2001 and 15 August 2007, *Bull. Seismol. Soc. Am.*, *100*, 969–994, doi:10.1785/0120090274.

Lundgren, P., M. Protti, A. Donnellan, M. Heflin, E. Hernandez, and D. Jefferson (1999), Seismic cycle and plate margin deformation in Costa Rica: GPS observations from 1994 to 1997, *J. Geophys. Res.*, *104*(B12), 28,915–28,926.

Miyazaki, S., K. M. Larson, K. Choi, K. Hikima, K. Koketsu, P. Bodin, J. Haase, G. Emore, and A. Yamagiwa (2004), Modeling the rupture process of the 2003 September 25 Tokachi-Oki (Hokkaido) earthquake using 1-Hz GPS data, *Geophys. Res. Lett.*, *31*, L21603, doi:10.1029/2004GL021457.

Newman, A. V., S. Y. Schwartz, V. Gonzáles, H. R. DeShon, J. M. Protti, and L. Dorman (2002), Along strike variability in the seismogenic zone below Nicoya Peninsula, Costa Rica, *Geophys. Res. Lett.*, *29*(20), 1977, doi:10.1029/2002GL015409.

Newman, A. V., J. M. Protti, V. M. Gonzalez, T. H. Dixon, S. Y. Schwartz, L. Feng, Z. Peng, J. Marshall, R. Malservisi, and S. E. Owen (2013), Success! Detailed pre-event analysis identified the slip area and magnitude of the Sept. 2012 M_w 7.6 Nicoya Earthquake, Abstract at the 2013 AGU Meeting of the Americas, Cancun, Mexico, 14–17 May 2013.

Nishenko, S. P. (1991), Circum-Pacific seismic potential: 1989–1999, *Pure Appl. Geophys.*, *135*(2), 169–259, doi:10.1007/BF00880240.

Norabuena, E., et al. (2004), Geodetic and seismic constraints on some seismogenic zone processes in Costa Rica, *J. Geophys. Res.*, *109*, B11403, doi:10.1029/2003JB002931.

Okada, Y. (1992), Internal deformation due to shear and tensile faults in a half-space, *Bull. Seismol. Soc. Am.*, *82*(2), 1018–1040.

Outerbridge, K. C., T. H. Dixon, S. Y. Schwartz, J. I. Walter, M. Protti, V. González, J. Biggs, M. Thorwart, and W. Rabbel (2010), A tremor and slip event on the Cocos-Caribbean subduction zone as measured by a global positioning system (GPS) and seismic network on the Nicoya Peninsula, Costa Rica, *J. Geophys. Res.*, *115*, B10408, doi:10.1029/2009JB006845.

Pacheco, J. F., and L. R. Sykes (1992), Seismic moment catalog of large shallow earthquakes, 1900 to 1989, *Bull. Seismol. Soc. Am.*, *82*(3), 1306–1349.

Protti, M., et al. (1995), The March 25, 1990 (M_w = 7.0, M_L = 6.8), earthquake at the entrance of the Nicoya Gulf, Costa Rica: Its prior activity, foreshocks, aftershocks, and triggered seismicity, *J. Geophys. Res.*, *100*(B10), 20,345–20,358, doi:10.1029/94JB03099.

Protti, M., M. F. Güendel, and E. Malavassi (2001), *Evaluación del potencial sísmico de la Península de Nicoya*, pp. 144, 1st ed., Ed. Fund. Univ. Nac., Heredia, Costa Rica.

Protti, M., V. González, J. Freymueller, and S. Doelger (2012), Isla del Coco, on Cocos Plate, converges with San Andres Island, on the Caribbean Plate, at 78mm/yr, *Rev. Biol. Trop.*, *60*(3), 33–41, (Int. J. Trop. Biol. ISSN-0034-7744).

Schwartz, S. Y., and J. M. Rokosky (2007), Slow slip and seismic tremor at circum-Pacific subduction zones, *Rev. Geophys.*, *45*, RG3004, doi:10.1029/2006RG000208.

Shimazaki, K., and T. Nakata (1980), Time-predictable recurrence model for large earthquakes, *Geophys. Res. Lett.*, *7*(4), 279–282.

Spinelli, G. A., and D. M. Saffer (2004), Along-strike variations in underthrust sediment dewatering on the Nicoya margin, Costa Rica related to the updip limit of seismicity, *Geophys. Res. Lett.*, *31*, L04613, doi:10.1029/2003GL018863.

Walter, J. I., S. Y. Schwartz, J. M. Protti, and V. González (2011), Persistent tremor within the northern Costa Rica seismogenic zone, *Geophys. Res. Lett.*, *38*, L01307, doi:10.1029/2010GL045586.

Wei, S., R. Graves, D. Helmberger, J. P. Avouac, and J. Jiang (2012), Sources of shaking and flooding during the Tohoku-Oki earthquake: A mixture of rupture styles, *Earth Planet. Sci. Lett.*, *333*, 91–100, doi:10.1016/j.epsl.2012.04.006.

Ye, L., T. Lay, and H. Kanamori (2013), Large earthquake rupture process variations on the Middle America megathrust, *Earth and Planet. Sci. Lett.*, *381*(0), 147–155.

Yue, H., and T. Lay (2011), Inversion of high-rate (1 sps) GPS data for rupture process of the 11 March 2011 Tohoku earthquake (M_w 9.1), *Geophys. Res. Lett.*, *38*, L00G09, doi:10.1029/2011GL048700.

Yue, H., and T. Lay (2013), Source rupture models for the M_w 9.0 2011 Tohoku earthquake from joint inversions of high-rate geodetic and seismic data, *Bull. Seismol. Soc. Am.*, *103*(2b), 1242–1255, doi:10.1785/0120120119.

Zumberge, J. F., M. B. Heflin, D. C. Jefferson, M. M. Watkins, and F. H. Webb (1997), Precise point positioning for the efficient and robust analysis of GPS data from large networks, *J. Geophys. Res.*, *102*(B3), 5005–5017.